JACS
JOURNAL OF THE AMERICAN CHEMICAL SOCIETY
Article
Cite This: J. Am. Chem. Soc. 2018, 140, 12484−12492
pubs.acs.org/JACS

Cationic Ordering Coupled to Reconstruction of Basic Building Units during Synthesis of High-Ni Layered Oxides

Ming-Jian Zhang,[†,‡] Gaofeng Teng,[‡] Yu-chen Karen Chen-Wiegart,[§,∥] Yandong Duan,[†,‡] Jun Young Peter Ko,[⊥] Jiaxin Zheng,[‡] Juergen Thieme,[∥] Eric Dooryhee,[∥] Zonghai Chen,[#] Jianming Bai,[*,∥] Khalil Amine,[*,#] Feng Pan,[*,‡] and Feng Wang[*,†]

[†]Sustainable Energy Technologies Department, Brookhaven National Laboratory, Upton, New York 11973, United States
[‡]School of Advanced Materials, Peking University, Shenzhen Graduate School, Shenzhen 518055, China
[§]Department of Materials Science and Chemical Engineering, Stony Brook University, Stony Brook, New York 11794, United States
[∥]National Synchrotron Light Source II, Brookhaven National Laboratory, Upton, New York 11973, United States
[⊥]Cornell High Energy Synchrotron Source, Cornell University, Ithaca, New York 14853, United States
[#]Electrochemical Technology Program, Chemical Sciences and Engineering Division, Argonne National Laboratory, Argonne, Illinois 60439, United States

Supporting Information

ABSTRACT: Metal (M) oxides are one of the most interesting and widely used solids, and many of their properties can be directly correlated to the local structural ordering within basic building units (BBUs). One particular example is the high-Ni transition metal layered oxides, potential cathode materials for Li-ion batteries whose electrochemical activity is largely determined by the cationic ordering in octahedra (e.g., the BBUs in such systems). Yet to be firmly established is how the BBUs are inherited from precursors and subsequently evolve into the desired ordering during synthesis. Herein, a multimodal in situ X-ray characterization approach is employed to investigate the synthesis process in preparing Li-$Ni_{0.77}Mn_{0.13}Co_{0.10}O_2$ from its hydroxide counterpart, at scales varying from the long-range to local individual octahedral units. Real-time observation corroborated by first-principles calculations reveals a topotactic transformation throughout the entire process, during which the layered framework is retained; however, due to preferential oxidation of Co and Mn over Ni, significant changes happen locally within NiO_6 octahedra. Specifically, oxygen loss and the associated symmetry breaking occur in NiO_6; as a consequence, Ni^{2+} ions become highly mobile and tend to mix with Li, causing high cationic disordering upon formation of the layered oxides. Only through high-temperature heat treatment, Ni is further oxidized, thereby inducing symmetry reconstruction and, concomitantly, cationic ordering within NiO_6 octahedra. Findings from this study shed light on designing high-Ni layered oxide cathodes and, more broadly, various functional materials through synthetic control of the constituent BBUs.

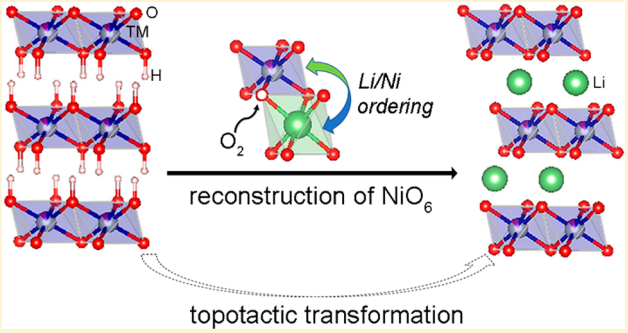

1. INTRODUCTION

In nature, the crystal structures and properties of solids, such as metal (M) oxides, are based on the long-range ordered arrangement of the basic building units (BBUs), MO_n polyhedra. This is the case in most of materials, whether naturally formed or synthesized. However, particular properties are very often rooted in the local symmetry and ordering of MO_n polyhedra, which dictates how the constituent cations are ordered within MO_n. For example, in the representative ferroelectric material $BaTiO_3$, the large ferroelectric polarization arises from the symmetry distortion of TiO_6 octahedra under an electric field.[1] In the nonlinear optical material LiB_3O_5, the large nonlinear optical effect comes from the asymmetric vibrations of the BO_3 unit under an optic-electric field.[2] In the representative layered cathode materials, the Li^+ de/intercalation during electrochemical cycling involves a symmetry change of LiO_n polyhedra from octahedra, to tetrahedra, then to octahedra (o-t-o).[3,4] During the process, the retention of high CoO_6 symmetry is crucial to the high electrochemical activity;[5] in contrast, due to the Jahn−Teller activity of Ni^{3+}, $LiNiO_2$ behaves fundamentally differently from $LiCoO_2$ even though their host structures are identical and Co and Ni have similar ionic sizes.[6] Examples from literature show that the local symmetry of MO_n polyhedra greatly affects, and even dominates the functionality of ferroelectric, ferromag-

Received: June 11, 2018
Published: August 31, 2018

DOI: 10.1021/jacs.8b06150
J. Am. Chem. Soc. 2018, 140, 12484−12492

netic, thermoelectric, nonlinear optical, superconducting, and battery materials.[7−9] Therefore, understanding how BBUs are inherited from precursors and subsequently evolve into the desired ordering during synthesis may enable synthetic design of new functional materials.

Transition metal (TM) oxides are arguably the most important solid materials in various applications because they are naturally abundant and exhibit numerous structures and properties applicable to optics, electronics, magnetism, catalysis, and energy conversion/storage fields.[10−15] Notably, the multi-cation layered oxides $LiNi_xMn_yCo_zO_2$ (generally called NMC; space group (SG): *R*-3*m*) has been widely applied as cathodes in lithium-ion batteries, for electric vehicle and other large-scale applications.[16−20] To further boost Li storage capacity, research efforts are now increasingly focused on developing NMC with a high Ni content (i.e., $1 - x \geq 0.7$).[21,22] However, cycling stability and safety are often compromised due to the high reactivity of Ni and the structural reconstruction on the particle surface.[23−26] Significant efforts have been given to surface or bulk modifications of electrodes in order to improve their electrochemical performance.[27,28] However, implementation of these strategies to make NMC oxides with desired structure and properties is often difficult due to the complexity of the synthesis reactions, especially for making such a multi-cation quaternary system. In addition, as Ni loading increases, cationic disordering in octahedral sites (i.e., Li^+/Ni^{2+} mixing) degrades electrochemical activity;[29] this has been attributed to the slow oxidation of Ni from Ni^{2+} to Ni^{3+} during synthesis.[30,31] So far, most of efforts have been focused on accelerating Ni oxidation through flowing O_2 atmosphere, adding excessive Li source, or preoxidation of precursors during synthesis, aiming at better Li/Ni ordering.[32−36] However, efficient oxidation of Ni during synthesis has been challenging, and it is still unclear how the oxidation from Ni^{2+} to Ni^{3+} occurs and, consequently, impacts the Li^+/Ni^{2+} ordering during synthesis.

For large-scale industrial applications, NMC oxides are generally prepared through solid-state synthesis, using layered hydroxides (SG: *P*-3*m*1) as precursors. Basically these two have similar layered structures, wherein the TM layers are either composed of edge-sharing $TM(OH)_6$ octahedra or TMO_6 octahedra.[20] Investigating how the TMO_6 octahedra are inherited from hydroxide precursors and subsequently evolve is vitally important for the synthetic design of layered cathode materials with desired high Li/TM ordering.[37−40] Recently, the long-range structural evolution of NMC, especially the cationic ordering, has been investigated using in situ high energy X-ray diffraction (XRD) techniques.[29,41] Nevertheless, the local structural/chemical evolution at the scale of individual TMO_6 octahedra during synthesis is still not well understood due to the technical challenges in structural characterization at such a fine scale.

In this work, multimodal synchrotron X-ray techniques including diffraction, total scattering and absorption spectroscopy were employed to track the long-/short-range structural evolution and, locally, the oxidation of all constituent TM cations in TMO_6 octahedra during the synthesis of $LiNi_{77}Mn_{0.13}Co_{0.10}O_2$ (NMC771310) from hydroxide precursors ($Ni_{0.77}Mn_{0.13}Co_{0.10}(OH)_2$). In situ observation coupled with first-principles calculations revealed a topotactic transformation process wherein the layered framework was retained, but significant change occurred locally within individual TMO_6 octahedra. Specifically, local symmetry breaking and reconstruction of NiO_6 octahedra dominated Li/Ni mixing/ordering processes. Such findings shed light on the synthetic design of stoichiometric high-Ni layered oxide cathodes and other functional materials through tuning the constituent BBUs.

2. EXPERIMENTAL SECTION

2.1. Synthesis of NMC771310. The hydroxide precursor with nominal composition of $Ni_{0.77}Mn_{0.13}Co_{0.10}(OH)_2$ for preparing NMC771310 was synthesized via a modified coprecipitation method in a continuously stirred tank reactor (CSTR).[42] First, a 2-mol/L solution of $NiSO_4{\cdot}6H_2O$, $MnSO_4{\cdot}5H_2O$, and $CoSO_4{\cdot}7H_2O$ (Ni: Co: Mn = 77:13:10 molar ratio), was prepared as the starting material for the coprecipitation process. During the reaction, the solution was continuously pumped into a 4-L CSTR that had been filled with distilled water and heated to 55 °C. The water was purged with nitrogen while stirring at a rate of 1000 rpm. A solution of aqueous ammonia was continuously dripped into the sealed reactor. The pH was fixed at 11.5 by adding an aqueous solution of sodium hydroxide using a pH controller/pump. The final precursor particles were washed, filtered, and dried. For preparing NMC layered oxides, the obtained precursor was mixed with 5% excessive LiOH by grinding for 1 h. This mixture was then used in various in situ and ex situ calcination experiments. For ex situ measurements, 10 samples were prepared by calcining the mixture of $(Ni_{0.77}Mn_{0.13}Co_{0.10})(OH)_2$ and LiOH at room temperature (RT), 150, 200, 250, 300, 400, 500, 700, 800, and 850 °C for 30 min, respectively.

2.2. In Situ High-Energy XRD Measurements. Time-resolved high-energy XRD patterns were collected from the mixture of $(Ni_{0.77}Mn_{0.13}Co_{0.10})(OH)_2$ and LiOH during calcination, at Sector 28-ID-2 of the National Synchrotron Light Source II (NSLS-II) at Brookhaven National Laboratory (BNL). The wavelength of the X-ray beam was 0.18266 Å. The mixture was loaded onto a piece of Al_2O_3 cloth, which had been emerged in a LiOH saturated solution and dried in an oven at 80 °C before being used to compensate the Li loss at high temperature. Then the sample was placed in a furnace (Linkam TS 1500) vertically, with a window perpendicular to the X-ray beam. The sample was then heated in air by following the temperature profile shown in Figure S1 of the Supporting Information (SI). During the calcination, a 2D X-ray detector was deployed to collect the XRD patterns. The focused spot size is 0.5 mm (horizontal) × 0.5 mm (vertical). Ex situ XRD patterns were acquired for the hydroxide precursors without Li source calcined at 850 °C for 30 min and $LiNiO_2$ at the F2 station of Cornell High Energy Synchrotron Source (CHESS) at Cornell University with the wavelength of 0.295264 Å.

2.3. Refinement of XRD Data. Rietveld refinements of XRD patterns were carried out using the General Structure Analysis Software (GSAS) package with the EXPGUI interface.[43,44] $Ni(OH)_2$ (SG: *P*-3*m*1) and $LiCoO_2$ (SG: *R*-3*m*) were employed as the structural models for initial hydroxides and the final layered oxides products, respectively. The global refining parameters included background coefficients, peak shape parameters, lattice parameters, and the weights of different structures. For the layered oxides structure, the positional parameter of O (6c); the fractional factors of all Li, Ni, Co, and Mn; and isotropic atomic displacement parameters (U_{iso}) were refined. The chemical formula $(Li_{1-x}Ni_x)_{3b}(Ni_{0.77-0.23x-0.77y}Mn_{0.13\ 0.13x-0.13y}Co_{0.10+0.10x-0.10y})_{3a}O_2$ was followed. That is, the total occupancy of Li and Ni at 3b sites and the total occupancy of Ni, Co, Mn, and Li at 3a sites were constrained to be unity; the atomic ratio of Ni: Mn: Co was constrained as stoichiometric, that is, 0.77:0.13:0.10. The U_{iso} of all elements sharing the same crystallography position was set to be equivalent.

2.4. In Situ High-Energy X-ray Total Scattering Measurements and Pair Distribution Function (PDF) Analysis. Temperature-resolved high energy X-ray total scattering measurements were also performed at Sector 28-ID-2 of NSLS-II at BNL. The wavelength of the X-ray beam was 0.18545 Å. The mixture of $Ni_{0.77}Mn_{0.13}Co_{0.10}(OH)_2$ and LiOH was pressed into pellets for the measurements. To ensure the consistency of the experimental results,

DOI: 10.1021/jacs.8b06150
J. Am. Chem. Soc. 2018, 140, 12484−12492

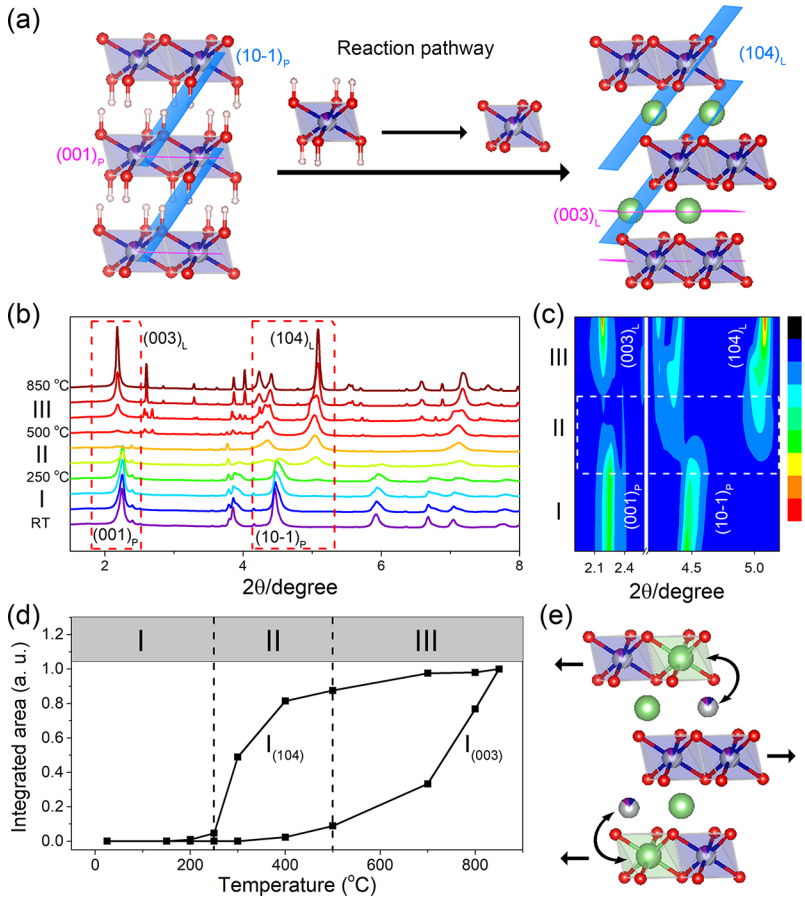

Figure 1. Structural transformation during solid-state synthesis of the layered $LiNi_{0.77}Mn_{0.13}Co_{0.10}O_2$ (NMC771310) from the hydroxide precursor $Ni_{0.77}Mn_{0.13}Co_{0.10}(OH)_2$. (a) Schematic of the transformation from layered hydroxide precursors (*P*-3*m*1) to layered oxides (*R*-3*m*), and the corresponding change in the BBUs, from initial $TM(OH)_6$ to the TMO_6 octahedra. (b) Temperature-resolved in situ synchrotron XRD patterns, showing three sequential stages during the entire synthesis process: I (below 250 °C), II (250−500 °C), and III (above 500 °C). (c) Contour plot of selected regions in XRD patterns (marked with red dashed rectangles). (d) Evolution of integrated intensities of (003) and (104) peaks (denoted as $I_{(003)}$ and $I_{(104)}$, being normalized to their corresponding values at 850 °C), which reflects the behaviors of cationic disordering/ordering (by $I_{(003)}$) and Li insertion (by $I_{(104)}$) as the temperature increases. (e) Schematic of atomic rearrangement, interlayer gliding, and Li/Ni mixing (illustrated by arrows) in the intermediate ($Ni_{0.77}Mn_{0.13}Co_{0.10}(OH_{1-x}Li_y)_2$) during Stage II.

the same temperature profile (Figure S1) was used. Ex situ total scattering experiments were also performed for 10 samples prepared at different temperatures, for comparing with the in situ total scattering data. The ex situ data were recorded at the X-ray wavelength of 0.18266 Å. The PDFs, G(r), were extracted by direct Fourier transform of total scattering data using PDFgetX2 to Q_{max} = 20 $Å^{-1}$.[45]

The PDF G(r) is the Fourier transformed form of total scattering data (S(Q), including both Bragg scattering that originates from long-range periodicity and diffuse scattering that originates from local distortion, which can provide information both in the long-range and in the short-range.[46−49] Therefore, PDF has unique advantages in analyzing materials with limited structural coherence length.[50]

$$G(r) = \frac{2}{\pi}\int_0^\infty Q[S(Q) - 1]\sin Qr\, dQ \quad (1)$$

$$S(Q) = \int_{-\infty}^{+\infty} \frac{b_i b_j}{\langle b\rangle^2}\rho(r_{ij})\frac{\sin(Qr_{ij})}{Qr_{ij}}d\rightarrow_{r_{ij}} \quad (2)$$

wherein b_i and b_j are the scattering lengths for atom i and j, respectively; $\langle b\rangle$ is the average scattering length over all atoms; r_{ij} is the interatomic distance between atoms i and j; $\rho(r)$ is the pair density; and Q is the scattering vector.

2.5. In Situ X-ray Absorption Near-Edge (XANES) Measurements. In situ XANES spectra were collected at beamline 5-ID of NSLS-II at BNL. The sample preparation procedure is similar to the in situ XRD measurements. To decrease the strong X-ray absorption of TM elements by the thick samples, a diluted solution for the mixture of $Ni_{0.77}Mn_{0.13}Co_{0.10}(OH)_2$ and LiOH was used. The dilute solution was prepared by dispersing 30 mg of the mixture into 30 mL of ethanol. To ensure the consistency of the experiment results, the same temperature profile (Figure S1) was used. Energy calibration of each spectrum was performed by aligning the first derivative maximum of reference K-edge XANES spectra of Mn, Co, and Ni collected simultaneously from the metal foils in the reference channel. $LiNiO_2$ was measured as the standard material for Ni^{3+}.

2.6. Fitting of XANES Spectra. The linear combination fitting for Ni, Co, and Mn K-edge XANES spectra was performed using Athena software.[51] The fitting range is from −20 to 30 eV (relative to the energy of the edge; E_0). When fitting the Ni K-edge spectra, the first spectra at RT and $LiNiO_2$ were used as standards for Ni^{2+} and Ni^{3+}. When fitting the Co and Mn K-edge spectra, the first spectra at RT and the last spectra after cooling down were used as references for Co^{2+}/Mn^{2+} and Co^{3+}/Mn^{4+}, respectively.

2.7. Scanning Electron Microscopy (SEM) and Thermogravimetric Analysis (TGA). A JEOL 7600F scanning electron microscope was used to record SEM images for the hydroxide precursors and the final layered oxides. TGA data and differential scanning calorimetry (DSC) data of hydroxide precursors were collected on a TGA/DSC1 system at a heating rate of 5 °C/min under air flow.

DOI: 10.1021/jacs.8b06150
J. Am. Chem. Soc. 2018, 140, 12484−12492

2.8. Ab Initio Computation. All calculations were performed with the plane-wave projector-augmented wave method,[52,53] as implemented in the Vienna ab initio simulation package.[54,55] The Perdew-Burke-Ernzerhof (PBE) form of generalized gradient approximation (GGA) was chosen as the exchange-correlation potential.[56,57] The PBE+*U* approach with spin polarization was employed to take account of the strong on-site Coulomb interaction (*U*), presented in the localized 3d electrons of Ni, Mn, and Co with U values being set as 6.7, 4.2, and 4.9 eV,[58−60] respectively. The cutoff energy for the plane wave was 520 eV. The integration in the Brillouin zone was done on a set of K-points determined by the Monkhorst and Pack theme, 6 × 3 × 3. Convergence was assumed when the total energy difference was less than 10^{-4} eV, and the residual force was less than 0.01 eV/Å between cycles of self-consistent iterations. Minimum energy pathways were calculated with the climbing-image nudged elastic method (cNEB).

To simplify the calculations, a multilattice structure NMC71515 model with a similar composition to NMC771310 was constructed to perform the calculations. In the calculations, a nearby Li ion was also removed to produce a nearby vacancy, and an O ion was removed to produce 5-coordinated Ni^{2+}. This state was set as the initial state after the decomposition of the $Ni(OH)_2$ part in the framework. Then a final state was constructed when the symmetry-breaking Ni^{2+} was migrated into the nearby vacancy. The minimum energy migration pathway and the relevant system energies were calculated. The migration of Ni^{2+} left a vacancy in the TM layer. A pathway was also calculated for the migration of neighboring Li^+ from the Li layer to this vacancy in the TM layer after the migration of Ni^{2+}. The migration pathway of Ni^{2+} without the symmetry breaking of NiO_6 octahedra was also calculated for comparison.

3. RESULTS AND DISCUSSION

3.1. Topotactic Transformation. In this study, the precursor $Ni_{0.77}Mn_{0.13}Co_{0.10}(OH)_2$ (SG: *P*-3*m*1) has a very similar layered structure as that of the final product $Li(Ni_{0.77}Mn_{0.13}Co_{0.10})O_2$ (denoted as NMC771310), both being composed of edge-sharing $TM(OH)_6$ and TMO_6 octahedra respectively, as illustrated in Figure 1a. The structural evolution during the synthesis process was followed by temperature-resolved in situ synchrotron XRD patterns (see the details in the Experimental Section 2.2). The main results are given in Figure 1b−d. Overall, the hydroxide precursors undergo three different stages as temperature increases (Figures 1b and S2−S4): I (below 250 °C), II (250−500 °C), and III (above 500 °C). In Stage I, no new peaks appear, which indicates that the layered structure of the hydroxides (*P*-3*m*1) is preserved. The whole pattern, represented by the $(001)_P$ and $(10-1)_P$ peaks, shifts to higher angles to different extents, hinting at an anisotropic lattice shrink. Stage II involves abrupt phase transformation. In this stage, the peaks of the hydroxides rapidly vanish, and a new $(104)_L$ peak, associated with layered oxides (with Li inserted in the structure; as illustrated in Figure 1a), begins to appear at about 250 °C, indicating the onset of the transition from the initial hydroxide to an intermediate $Ni_{0.77}Mn_{0.13}Co_{0.10}(OH_{1-x}Li_y)_2$. As temperature continues to increases, the $(104)_L$ peak grows rapidly with more Li insertion, and the $(003)_L$ peak starts to appear at around 400 °C. In the layered structure, the structure factor of the $(003)_L$ peak is proportional to the difference between the scattering factors of ions in the Li and TM layers, and will be zero when the distribution of Li and TM cations is totally random.[61] Therefore, the emergence of the small $(003)_L$ peak implies the formation of the layered structure (*R*-3*m*), but with serious Li/TM mixing at octahedral sites.[41] In Stage III (above 500 °C), both $(003)_L$ and $(104)_L$ peaks grow up quickly and become narrower as temperature increases, suggesting an increase of crystallinity and a fast Li/TM ordering process in the newly formed layered structure. Correspondingly, TM ions in Li layers migrate to TM layers while Li ions in TM layers migrate to Li layers.[41] The trend of changes can be better viewed in the contour map (Figure 1c).

From the evolution of the intensity of $(003)_L$ and $(104)_L$ peaks (denoted as $I_{(003)}$, $I_{(104)}$), plotted in Figure 1d, we learn about the detailes of Li insertion, and the related Li/TM mixing/ordering processes. Swift Li insertion mainly happens in Stage II, as indicated by a rapid increase in $I_{(104)}$, by 88%. The Li-deficient layered oxide is already formed in this stage, through Li^+/H^+ exchange in the hydroxide precursor, leading to the formation of an intermediate $Ni_{0.77}Mn_{0.13}Co_{0.10}(OH_{1-x}Li_y)_2$. At the same time, the Li and TM cations are highly mixed, as indicated by the low value of $I_{(003)}$. In Stage III (above 500 °C), Li insertion slows down (as indicated by the gradual increase of $I_{(104)}$), but fast Li/Ni ordering occurs, as indicated by the rapid increase of $I_{(003)}$.

On the basis of the discussion above, Figure 1e presents the structure for the intermediate $Ni_{0.77}Mn_{0.13}Co_{0.10}(OH_{1-x}Li_y)_2$ observed in Stage II. In this stage, a significant amount of Li has been inserted into the structure, but highly mixed with Ni at octahedral sites. Interlayer gliding between neighboring TM layers occurs (driven by Li insertion); while the layered framework of the hydroxide precursor does not break down throughout the synthesis process, in contrast to the decomposition process reported in other types of precursors, such as acetate-based precursors.[41] This resembles a topotactic transformation process, as commonly observed during electrochemical intercalation in NMC layered cathodes, or traditional epitaxial or topotactic growth at high temperatures.[62,63] The observation on the topotactic transformation should be common during the solid-sate synthesis of NMC oxides from hydroxides (despite different compositions), which may explain why hydroxide precursors have been commonly used for preparing NMC oxides.

3.2. Dynamic Cationic Ordering within TMO_6 Octahedra. Results from in situ XRD analysis indicate that the overall framework (built on the edge-sharing octahedra) was preserved during the transformation from layered hydroxides to oxides. Nevertheless, details about the local structure/chemical evolution in the intermediates (as in Stage II) involving proton/Li^+ exchange, and the related cationic disordering (as shown in Figure 1e), could not be resolved from XRD alone. Therefore the local synchrotron X-ray probing technique, total scattering coupled with PDF analysis,[46−49] was also applied here to gain details about local structural evolution (using the same heating procedure as for in situ XRD, Figure S1).

Figure 2a shows the temperature-resolved X-ray PDF patterns obtained from Fourier transform of the total scattering data (see details in Section 2.4 and Figures S5 and S6).[50,64,65] Consistent with the XRD results above, the overall evolution of the in situ PDF patterns follows three stages (as labeled); but additional details about the structural ordering can be obtained from the PDF patterns. In the large-radius range (>20 Å, exceeding the range of 5 unit cells), the abrupt decrease of peak intensity in Stage I indicates the loss of long-range ordering of layered hydroxides (*P*-3*m*1). As temperature continues to increase (in Stage II), new long-range ordering gradually builds up, corresponding to a phase transformation to layered oxides (*R*-3*m*). From Stage II to Stage III, the

DOI: 10.1021/jacs.8b06150
J. Am. Chem. Soc. 2018, 140, 12484−12492

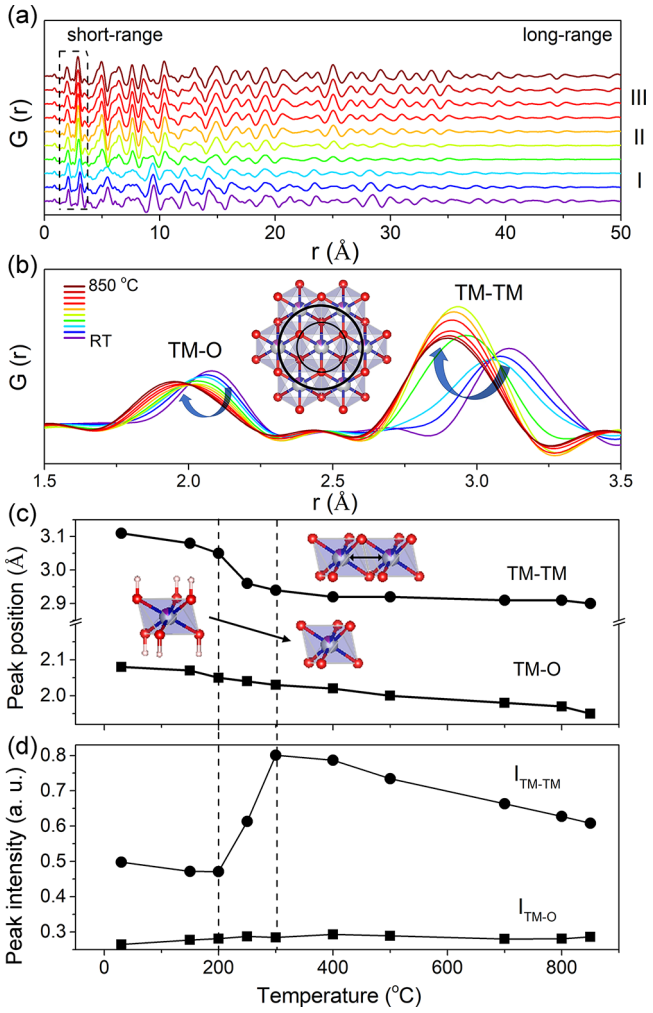

Figure 2. Dynamic process of local structural ordering within TMO_6 octahedra during synthesis of NMC771310. (a) Temperature-resolved in situ PDF patterns in a wide r range, showing changes in long-range and short-range ordering. (b) Enlarged low r range (r = 1.5−3.5 Å, marked by the dashed square in (a)), wherein the two peaks at 1.6−2.4 Å, and 2.5−3.5 Å correspond to the scattering signals of TM−O and TM−TM atomic pairs, respectively. (c) Positions of TM−O and TM−TM peaks as a function of temperature (curves with squares and circles, respectively), showing the evolution of the interatomic distances. (d) Integrated intensity of TM−O and TM−TM peaks (curves with squares and circles, respectively; denoted I_{TM-O} and I_{TM-TM}) as a function of temperature.

overall shape of the patterns is preserved. Intensity gradually increases as temperature increases, especially in the long-range, which hints at the enhancement of long-range ordering with temperature.

The change in the small r range (<3.5 Å) is barely observable. Therefore, patterns in the selected r region (r = 1.5−3.5 Å) are enlarged (Figure 2b), mainly including scattering signals of the TM−O and TM−TM pairs within a local domain consisting of 7 edge-sharing TMO_6 octahedra in TM layers illustrated in the inset of Figure 2b. Li−O and Li−TM atomic pairs also contribute to these two peaks, but their contribution is negligibly small due to the small scattering power of Li (~1/28 of Ni).[66] Clearly, the positions of the two peaks shift to low r direction, indicating that TM−O bond length and TM−TM interatomic distance are both shortening as the temperature increases. The broadening of two peaks below 200 °C, the TM−O peak in particular (also shown by the peak width in Figure S6), could be due to the decreasing symmetry in the TMO_6, associated with preferential oxidation of Co and Mn (identified via XANES analysis as discussed below).

To quantify the temperature dependence of the local structural evolution, the positions of the TM−O and TM−TM peaks were determined (Figure 2c and Table S2). The position of the TM−O peak gradually decreases from 2.08 to 1.95 Å as temperature increases, indicating that the TM−O bond length is continuously decreasing as a result of the TM oxidation. Unlike the TM−O case, the TM−TM peak shifts slowly to low r direction below 200 °C, then abruptly from 200 to 300 °C (by ~0.1 Å), which is followed by a gradual shift above 300 °C. The change in TM−TM peak should also be related to the oxidation of TMs. It is not solely related to the change in the TM−O bond length (a decrease by only ~0.01 Å between 200 to 300 °C), but also affected by the change in the O−TM−O bond angle, as shown in the inset of Figure 2c. So, in contrast to the subtle change in the TM−O bond length, the TM−TM interatomic distance decreases abruptly, by a factor of ~ 10, mainly due to the increase of O−TM−O bond angle in TMO_6 octahedra (from 82° to 86°; see Table S1). Such a large change in the TM−TM distance is related to the phase transformation from the hydroxide to the layered phase. Correspondingly, there is a quick increase of integrated intensity of TM−TM peak (I_{TM-TM}) and a much smaller increase in the intensity of the TM−O peak (I_{TM-O}). A similar trend was observed in the ex situ PDF (Figure S5). In general, the intensity of a certain peak is determined by the atomic densities.[64,65] Therefore, it is affected by the change of unit cell volume. The atomic ratio of O/TM is 1 in the initial hydroxide phase since six neighboring O atoms and six neighboring TM atoms surround the center TM atom (inset of Figure 2a). Therefore, it appears that the fast increase in I_{TM-TM} is related to the abrupt decrease of the TM−TM distance (corresponding to fast increase of the atomic density). But the change in the local structure is very complex, involving proton/Li^+ exchange, and the related cationic oxidation/reordering, and so needs further analysis. In addition, thermal effect also needs to be considered, as shown by the difference between in situ and ex situ PDF results (Figure S6).

In brief, the local structural changes within TMO_6 octahedra, including the variations of bond lengths and angles, and the atomic density increase, should be closely related to the site-dependent oxidation of cations in the TMO_6 octahedra. Nevertheless, the scattering factors of the three types of TMs (Ni, Mn, Co) to X-ray are similar, so the oxidation of Ni, Mn, Co cannot be distinguished by PDF. In addition to the preferential oxidation, cationic disordering, oxygen vacancies (and so symmetry breaking of the octahedra) should also be involved. To better understand of the local cationic oxidation and ordering in TMO_6 octahedra (involving Ni, Mn, Co), elemental-specific XANES analysis was carried out (see below).

3.3. Preferential Oxidation within TMO_6 Octahedra.

As illustrated in Figure 3a, there are three types of $TM(OH)_6$ in the precursors, namely $(Ni^{2+})(OH)_6$, $(Co^{2+})(OH)_6$, and $(Mn^{2+})(OH)_6$, which will turn into $(Ni^{3+})O_6$, $(Co^{3+})O_6$, and $(Mn^{4+})O_6$ upon formation of layered oxides. PDF analysis can only provide information about the averaged evolution in TMO_6 octahedra, but is incapable of differentiating three TMs: Ni, Mn, and Co. Therefore, in situ XANES experiments were

DOI: 10.1021/jacs.8b06150
J. Am. Chem. Soc. 2018, 140, 12484−12492

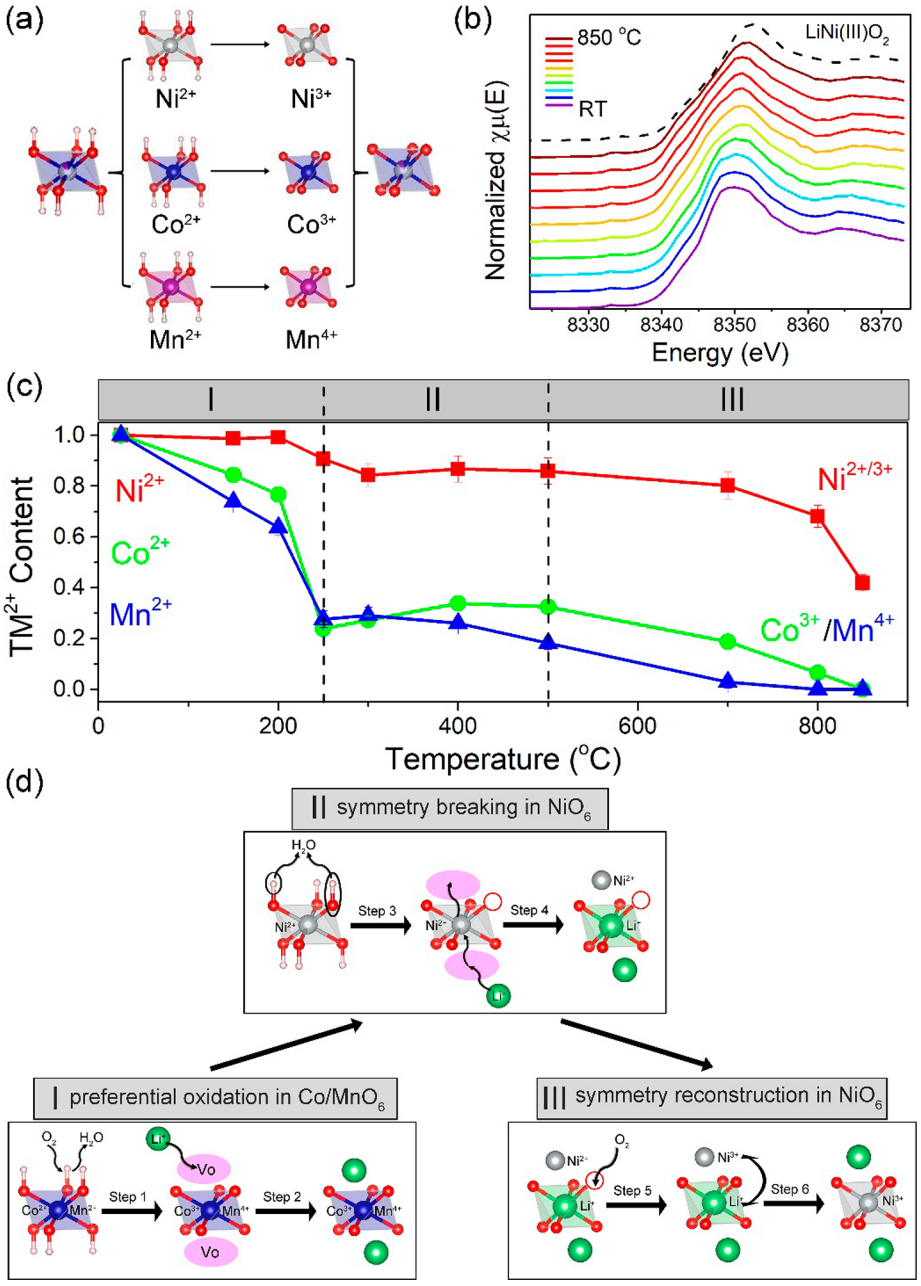

Figure 3. Oxidation dynamics of constituent cations (Ni, Mn, Co) during synthesis of NMC771310. (a) Schematic of the transformation of the octahedra associated with the hydroxides, namely, $(Ni^{2+})(OH)_6$, $(Co^{2+})(OH)_6$, and $(Mn^{2+})(OH)_6$ into octahedra associated with the layered oxides, $(Ni^{3+})O_6$, $(Co^{3+})O_6$, and $(Mn^{4+})O_6$, which involves oxidation of the three constituent cations (Ni, Co, Mn). (b) In situ Ni K-edge XANES spectra, compared to the reference spectrum (black dashed curve) from $LiNi(III)O_2$ (with high purity; see Figure S7). The spectra of Mn and Co K-edges were given in Figure S10. (c) Normalized Ni^{2+}, Co^{2+}, and Mn^{2+} contents as a function of temperature (by spectral fittings of temperature-resolved in situ XANES data; see the details in Section S2.4 of SI). (d) Schematic of the site-dependent cationic oxidation/reordering in octahedra, at the three sequential stages: I (below 250 °C); II (250 °C−500 °C); III (above 500 °C). The protons (H^+), Li^+ ions, and vacancies (V_O), are represented by magenta, green spheres, and purple ellipses, respectively.

performed on a single layer of particles dispersed on Al_2O_3 cloth (Figure S8 and S9), under the same calcination condition as in situ XRD and PDF. The main results are presented in Figures 3b and S10. As shown in Figure 3b, Ni K-edge shifts to higher energies, indicating oxidation of Ni (from initial Ni^{2+} in hydroxides) as the temperature increases. The shift to higher energy was also observed in Mn and Co K-edges (Figure S10), hinting at Co and Mn oxidation. However, their oxidation exhibits different behaviors than that of Ni, as shown by quantitative analysis given in Figure 3c (obtained via bicomponent linear fitting (Figure S11 and Tables S3-S5); see the details in Section S4 of SI).[51] The Ni^{2+} is not oxidized until the temperature increases to 250 °C (Stage I); it then slowly oxidizes in Stages II and III. In contrast, Co and Mn quickly oxidize almost fully to Co^{3+} and Mn^{4+} respectively, by the end of Stage I.

Combining results from XRD, PDF, and XANES analysis, we can now obtain details about the local change in each type of octahedra, as schematically illustrated in Figure 3d. In Stage I (<250 °C), preferential oxidation occurs to Co^{2+} and Mn^{2+},

DOI: 10.1021/jacs.8b06150
J. Am. Chem. Soc. 2018, 140, 12484−12492

and so $(Co^{2+})(OH)_6$ and $(Mn^{2+})(OH)_6$ octahedra turn into $(Co^{3+})O_6$ and $(Mn^{4+})O_6$. During this process, the local structure evolves sequentially, first involving the extraction of protons (H^+) in the presence of O_2, and then vacancies (Vo) between the neighboring TM layers are generated (in Step 1). As the reaction proceeds (Step 2), each $(Co^{3+})O_6$ octahedron carries one electron due to the loss of two protons. Once formed, this would lead to the instability of the structural framework of the initial hydroxide. As a result, a Li^+ ion will fill the vacancies surrounding the $(Co^{3+})O_6$ octahedron to balance the charge. This leads to an intermediate phase $(Ni^{2+})(OH)_{2-x}(Co^{3+}/Mn^{4+})(OLi)_x$. In contrast to the $(Co^{3+})O_6$ octahedra, the $(Mn^{4+})O_6$ octahedra are electroneutral, and thereby do not lead to the Li^+ insertion. This intermediate phase keeps the same structural framework as the initial hydroxide, as indicated by the similar XRD patterns and PDF patterns below 250 °C (Figures 1b and 2a). The results indicate that the shortening of the average TM−O bond length in this stage (see Figure 2c) comes from the oxidation of $(Co^{2+})(OH)_6$ and $(Mn^{2+})(OH)_6$ octahedra to $(Co^{3+})O_6$ and $(Mn^{4+})O_6$ octahedra, while such preferential oxidation causes the TM−O peak to broaden in the PDF (Figures 2b and S6), since there is no change in the Ni−O bond length, but large change in Mn/Co−O bond lengths.

In Stage II, there is further slight oxidation of Ni^{2+} (Figure 3c), but a large weight loss occurs (by around 15%) according to TGA studies (Section S5 in the SI), and correspondingly, a strong endothermic peak is observed at around 275 °C in the DSC curve, which indicates partial decomposition of the hydroxide precursor (Figure S12). Because Co^{2+} and Mn^{2+} oxidize nearly completely in Stage I, through a Li^+/H^+ exchange without weight loss, the $Ni(OH)_6$ octahedra should have decomposed, leading to $(Ni^{2+})O_{6-x}$ octahedra and H_2O, as illustrated in Step 3 in Figure 3d. To produce H_2O, both proton and OH^- should have dissociated from the $Ni(OH)_6$ octahedra, leading to asymmetric NiO_{6-x} octahedra and vacancies in the neighborhood. In the presence of Li source, quick Li insertion helps to stabilize the layered framework. However, the state may be highly metastable, due to the high concentration of vacancies (arising from the high Ni content). At this stage, the Ni^{2+} in the NiO_{6-x} octahedra may become mobile (discussed below through ab initio calculations), and so tends to migrate to the Li layer. Some of the Li may also go to the Ni site (as illustrated in Step 4 of Figure 3d). Significant amount of Li insertion is expected in Stage II, shown by the quick increase of $I_{(104)}$, (by 88% at 500 °C; Figure 1d). By the end of Stage II, the layered structure has already formed but with high Li/Ni mixing, namely $(Ni^{2+}/Ni^{3+}/Li^+)(OLi^+/Ni^{2+}/Vo)_{2-x}(Co^{3+}/Mn^{4+})(OLi^+)_x$, wherein each of the Co^{3+} and Mn^{4+} ions is strongly bonded with six O atoms. This indicates that the abrupt decrease in the symmetry of TMO_6 octahedra (as indicated by the TM-O peak broadening in Figures 2b, S6) may be explained by the formation of $(Ni^{2+})O_{6-x}$ (resulting from the dissociation of OH^-).

In Stage III (>500 °C), as temperature further increases, Ni is quickly oxidized, turning the asymmetric $(Ni^{2+})O_{6-x}$ octahedra to symmetric $(Ni^{3+})O_6$ (Step 5 in Figure 3d). Those Ni^{3+}, due to their much smaller radius (0.56 Å) than Li^+ (0.76 Å), tend to segregate from the Li layer (Step 6). This eventually leads to the ordered layered structure of $(Ni^{2+}/Ni^{3+})(OLi^+)_{2-x}(Co^{3+}/Mn^{4+})(OLi^+)_x$, which accounts for the fast increase of $I_{(003)}$ shown in Figure 1d.

The above discussion presents the change in each type of the TMO_6 octahedra during the entire synthesis process. In reality, the change in individual TMO_6 octahedra is not separated, but greatly intertwined with each other, as further discussed in Figure S13. Simply put, the preferential oxidation of $(Co^{2+})(OH)_6$ and $(Mn^{2+})(OH)_6$ octahedra in Stage I induces partial Li insertion, which is essential to maintaining the layered framework in the intermediate phase (Figure 1e). However, the slow oxidation of Ni triggers O loss and symmetry breaking of NiO_6 octahedra, which further leads to Li/Ni mixing. In Stage III (above 500 °C), further oxidation of Ni induces cationic ordering and, concomitantly, the symmetry reconstruction of the octahedra from NiO_{6-x} to NiO_6. The two processes couple with each other, eventually leading to a highly ordered structure.

3.4. Li/Ni Mixing Triggered by the Symmetry Breaking of NiO_6 Octahedra. On the basis of the above discussion, the symmetry breaking and reconstruction of NiO_6 octahedra play a dominant role in the reaction pathway during the synthesis of NMC771310. To better understand the process, ab initio calculations were made to determine the energy barriers for Ni migration in the presence of broken and reconstructed symmetry in NiO_6 octahedra (Figures 4 and S14). In the reconstructed symmetry case (black curve in Figure 4), Ni migration follows a pathway from octahedra to tetrahedra, then to octahedra (the o-t-o pathway), which is very similar to the Li migration pathway during the charge/discharge reported previously.[3,4] In the broken symmetry case (red curve in Figure 4), Ni migration follows a p-T-p pathway (from pentahedra to trigona to pentahedra) due to the missing O in NiO_6 octahedra. In this case, the energy difference before and after Ni migration is very small (0.31 eV), indicating that Ni migration is thermodynamically feasible. Notably, the activation energy barrier value is 0.57 eV, which is comparable to the theoretical values of Li migration (0.357−0.523 eV).[4,67] It indicates that Ni cations in NiO_{6-x} octahedra with broken symmetry migrate easily, similar to Li^+ ions. Results from the calculation suggest that Ni migration is facile in consideration of the kinetics even at lower temperature below 500 °C. In the reconstructed symmetry case (black curve in Figure 4), the activation energy barrier is 2.57 eV, about five times that of the symmetry breaking case, hinting a much lower migration capability.

In brief, the symmetry breaking due to the decomposition of $Ni(OH)_6$ into NiO_{6-x} and then reconstruction from NiO_{6-x} to NiO_6 octahedra determine the reaction pathway featuring Li/Ni mixing/ordering, from low to high temperatures. Accordingly, if one could avoid the symmetry breaking of NiO_6 octahedra by inhibiting the decomposition of $Ni(OH)_6$ octahedra, or making $Ni(OH)_6$ oxidize like $Co(OH)_6$ and $Mn(OH)_6$, Li/Ni mixing could be alleviated and even completely prevented in the initial phase transformation at around 250 °C. The idea could probably be implemented by providing a strong oxidizing environment or doping to lower the energy barrier for oxidation of $Ni(OH)_6$ octahedra. As a result, high-Ni layered oxides without Li/Ni mixing could be obtained even at low temperatures.

4. CONCLUSIONS

In summary, in situ multimodal synchrotron X-ray techniques were employed to study the long- and short-range chemical and structural evolution, down to individual BBUs during synthesis of high-Ni layered oxides. The real-time observation

DOI: 10.1021/jacs.8b06150
J. Am. Chem. Soc. 2018, 140, 12484−12492

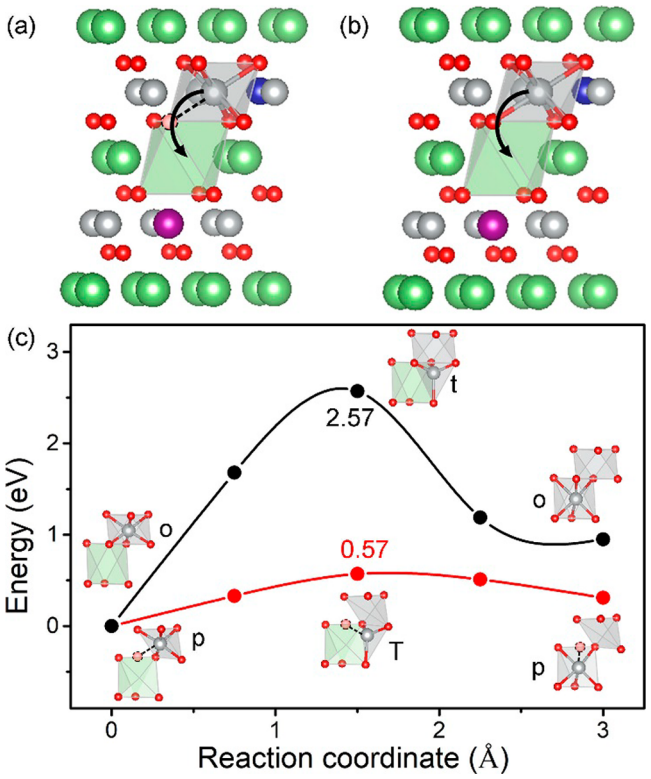

Figure 4. Energy barriers for Ni migration in the cases of the local symmetry breaking and reconstruction of NiO_6 octahedra via ab initio calculations. The simplified structural models for Ni migration from TM layer to Li layer with (a) broken symmetry and (b) reconstructed symmetry of NiO_6 octahedra. (c) Minimum energy pathways for Ni migration with the broken symmetry (bottom) and reconstructed symmetry (top) of NiO_6 octahedra. The black curve represents the case with the reconstructed symmetry, which shows a complete o-t-o migration pathway (from octahedra in TM layer to tetrahedra in Li layer, then to octahedra in Li layer). The red curve presents the case with broken symmetry, which shows a breaking o-t-o migration pathway (from pentahedra in TM layer to trigona in Li layer, then to pentahedra in Li layer, denoted as p-T-p).

revealed the local ordering and symmetry change within BBUs (i.e., octahedra) as synthesis progresses, namely, from the preferential oxidation of Co and Mn within $(Co/Mn)(OH)_6$ octahedra to the dissociation of OH^- from $Ni(OH)_6$ octahedra leading to asymmetric NiO_{6-x} octahedra, and finally to the oxidation and symmetry reconstruction of NiO_{6-x} octahedra resulting in NiO_6 octahedra. The preferential oxidation Co and Mn was identified to be a prerequisite for the topotactic transformation from hydroxides to oxides without destroying the layered framework. The symmetry breaking and reconstruction in NiO_6 octahedra played a crucial role in governing the reaction pathway, and the associated Li/Ni mixing/ordering processes. Through first-principles calculations, very low activation energy for Ni^{2+} migration, with a value comparable to that of Li^+ migration was predicted and attributed to the symmetry breaking of NiO_6 octahedra. Findings from this study highlight the vital importance of tuning the symmetry of NiO_6 octahedra during synthesis of high-Ni layered oxides of high structural ordering. The approach developed in this study may also be applied to in situ probing and synthetic control of structural ordering and properties in various other functional materials beyond energy storage materials.

■ ASSOCIATED CONTENT

Supporting Information

The Supporting Information is available free of charge on the ACS Publications website at DOI: 10.1021/jacs.8b06150.

The temperature profile, in situ XRD/PDF/XANES, ex situ PDF data analysis, SEM and TGA measurements, and computational results, appear in Figures S1−S14 and Tables S1−S5 (PDF)

■ AUTHOR INFORMATION

Corresponding Authors

*jmbai@bnl.gov
*amine@anl.gov
*panfeng@pkusz.edu.cn
*fwang@bnl.gov

ORCID

Zonghai Chen: 0000-0001-5371-9463
Khalil Amine: 0000-0001-9206-3719
Feng Pan: 0000-0002-8216-1339
Feng Wang: 0000-0003-4068-9212

Notes

The authors declare no competing financial interest.

■ ACKNOWLEDGMENTS

We thank Trevor A. Tyson and Sizhan Liu for discussions concerning PDF analysis. We thank Yusuf Celebi, John Trunk, and Garth Williams for technical support. This work was supported by the U.S. Department of Energy (DOE) Office of Energy Efficiency and Renewable Energy, Vehicle Technologies Office, Contract No. DE-SC0012704, the National Materials Genome Project (2016YFB0700600), and the Shenzhen Science and Technology Research Grants (JCYJ20150729111733470, JCYJ20151015162256516). Research at Argonne National Laboratory is supported by the DOE, Vehicle Technologies Office. Argonne National Laboratory is operated for DOE Office of Science by UChicago Argonne, LLC, under contract number DE-AC02-06CH11357. This research used the 5-ID (SRX), 28-ID-2 (XPD) beamlines of the National Synchrotron Light Source II, a DOE Office of Science User Facility operated for the DOE Office of Science by Brookhaven National Laboratory under Contract No. DE-SC0012704. SEM/EDX and TEM measurements carried out at the Center for Functional Nanomaterials, Brookhaven National Laboratory, were supported by the DOE, Office of Basic Energy Sciences, under Contract No. DE-SC0012704. The synchrotron XRD work conducted at the Cornell High Energy Synchrotron Source was supported by the National Science Foundation under award DMR-1332208. K. C.-W. acknowledges support from the Department of Materials Science and Chemical Engineering, the College of Engineering and Applied Sciences, and the Stony Brook University, as well as by Brookhaven National Laboratory under Contract No. DE-SC0012704.

■ REFERENCES

(1) Choi, K. J.; Biegalski, M.; Li, Y. L.; Sharan, A.; Schubert, J.; Uecker, R.; Reiche, P.; Chen, Y. B.; Pan, X. Q.; Gopalan, V.; Chen, L. Q.; Schlom, D. G.; Eom, C. B. *Science* **2004**, *306*, 1005.
(2) Savage, N. *Nat. Photonics* **2008**, *2*, 380.
(3) Lee, J.; Urban, A.; Li, X.; Su, D.; Hautier, G.; Ceder, G. *Science* **2014**, *343*, 519.

DOI: 10.1021/jacs.8b06150
J. Am. Chem. Soc. 2018, 140, 12484−12492

(4) Wei, Y.; Zheng, J.; Cui, S.; Song, X.; Su, Y.; Deng, W.; Wu, Z.; Wang, X.; Wang, W.; Rao, M.; Lin, Y.; Wang, C.; Amine, K.; Pan, F. *J. Am. Chem. Soc.* **2015**, *137*, 8364.
(5) Hertz, J. T.; Huang, Q.; McQueen, T.; Klimczuk, T.; Bos, J. W. G.; Viciu, L.; Cava, R. J. *Phys. Rev. B: Condens. Matter Mater. Phys.* **2008**, *77*, 075119.
(6) de Dompablo, M. E. A. Y.; Van der Ven, A.; Ceder, G. *Phys. Rev. B: Condens. Matter Mater. Phys.* **2002**, *66*, 064112.
(7) Damasceno, P. F.; Engel, M.; Glotzer, S. C. *Science* **2012**, *337*, 453.
(8) Wang, P. F.; Yao, H. R.; Liu, X. Y.; Yin, Y. X.; Zhang, J. N.; Wen, Y. R.; Yu, X. Q.; Gu, L.; Guo, Y. G. *Sci. Adv.* **2018**, *4*, eaar6018.
(9) Wang, P. F.; Xin, H.; Zuo, T. T.; Li, Q.; Yang, X.; Yin, Y. X.; Gao, X.; Yu, X.; Guo, Y. G. *Angew. Chem., Int. Ed.* **2018**, *57*, 8178.
(10) Tokura, Y.; Nagaosa, N. *Science* **2000**, *288*, 462.
(11) Kalinin, S. V.; Spaldin, N. A. *Science* **2013**, *341*, 858.
(12) Rao, C. N. R.; Cheetham, A. K. *Science* **1996**, *272*, 369.
(13) Suntivich, J.; May, K. J.; Gasteiger, H. A.; Goodenough, J. B.; Shao-Horn, Y. *Science* **2011**, *334*, 1383.
(14) Yin, Q. S.; Tan, J. M.; Besson, C.; Geletii, Y. V.; Musaev, D. G.; Kuznetsov, A. E.; Luo, Z.; Hardcastle, K. I.; Hill, C. L. *Science* **2010**, *328*, 342.
(15) Chen, G.; Zhou, W.; Guan, D. Q.; Sunarso, J.; Zhu, Y. P.; Hu, X. F.; Zhang, W.; Shao, Z. P. *Sci. Adv.* **2017**, *3*, e1603206.
(16) Dunn, B.; Kamath, H.; Tarascon, J. M. *Science* **2011**, *334*, 928.
(17) Liu, C.; Li, F.; Ma, L. P.; Cheng, H. M. *Adv. Mater.* **2010**, *22*, E28.
(18) Scrosati, B.; Garche, J. *J. Power Sources* **2010**, *195*, 2419.
(19) Manthiram, A.; Song, B.; Li, W. *Energy Storage Materials* **2017**, *6*, 125.
(20) Li, W. D.; Song, B. H.; Manthiram, A. *Chem. Soc. Rev.* **2017**, *46*, 3006.
(21) Li, J. Y.; Li, W. D.; Wang, S. Y.; Jarvis, K.; Yang, J. H.; Manthiram, A. *Chem. Mater.* **2018**, *30*, 3101.
(22) Xu, J.; Lin, F.; Doeff, M. M.; Tong, W. *J. Mater. Chem. A* **2017**, *5*, 874.
(23) Manthiram, A.; Knight, J. C.; Myung, S. T.; Oh, S. M.; Sun, Y. K. *Adv. Energy Mater.* **2016**, *6*, 1501010.
(24) Chen, H. R.; Dawson, J. A.; Harding, J. H. *J. Mater. Chem. A* **2014**, *2*, 7988.
(25) Li, W.; Liu, X.; Celio, H.; Smith, P.; Dolocan, A.; Chi, M.; Manthiram, A. *Adv. Energy Mater.* **2018**, *8*, 1703154.
(26) Song, B. H.; Li, W. D.; Oh, S. M.; Manthiram, A. *ACS Appl. Mater. Interfaces* **2017**, *9*, 9718.
(27) Shi, J. L.; Qi, R.; Zhang, X. D.; Wang, P. F.; Fu, W. G.; Yin, Y. X.; Xu, J.; Wan, L. J.; Guo, Y. G. *ACS Appl. Mater. Interfaces* **2017**, *9*, 42829.
(28) Shi, J. L.; Zhang, J. N.; He, M.; Zhang, X. D.; Yin, Y. X.; Li, H.; Guo, Y. G.; Gu, L.; Wan, L. J. *ACS Appl. Mater. Interfaces* **2016**, *8*, 20138.
(29) Wang, D.; Kou, R.; Ren, Y.; Sun, C.-J.; Zhao, H.; Zhang, M.-J.; Li, Y.; Huq, A.; Ko, J. Y. P.; Pan, F.; Sun, Y.-K.; Yang, Y.; Amine, K.; Bai, J.; Chen, Z.; Wang, F. *Adv. Mater.* **2017**, *29*, 1606715.
(30) Reimers, J. N.; Rossen, E.; Jones, C. D.; Dahn, J. R. *Solid State Ionics* **1993**, *61*, 335.
(31) Ohzuku, T.; Ueda, A.; Nagayama, M. *J. Electrochem. Soc.* **1993**, *140*, 1862.
(32) Arai, H.; Okada, S.; Ohtsuka, H.; Ichimura, M.; Yamaki, J. *Solid State Ionics* **1995**, *80*, 261.
(33) Arai, H.; Okada, S.; Sakurai, Y.; Yamaki, J. *Solid State Ionics* **1997**, *95*, 275.
(34) Arai, H.; Okada, S.; Sakurai, Y.; Yamaki, J. *J. Electrochem. Soc.* **1997**, *144*, 3117.
(35) Delmas, C.; Croguennec, L. *MRS Bull.* **2002**, *27*, 608.
(36) Zhang, Q.; Su, Y.; Chen, L.; Lu, Y.; Bao, L.; He, T.; Wang, J.; Chen, R.; Tan, J.; Wu, F. *J. Power Sources* **2018**, *396*, 734.
(37) Liu, W.; Oh, P.; Liu, X.; Lee, M. J.; Cho, W.; Chae, S.; Kim, Y.; Cho, J. *Angew. Chem., Int. Ed.* **2015**, *54*, 4440.
(38) Rozier, P.; Tarascon, J. M. *J. Electrochem. Soc.* **2015**, *162*, A2490.
(39) Li, J.; Doig, R.; Camardese, J.; Plucknett, K.; Dahn, J. R. *Chem. Mater.* **2015**, *27*, 7765.
(40) Li, J.; Doig, R.; Liu, H. S.; Botton, G.; Dahn, J. R. *J. Electrochem. Soc.* **2016**, *163*, A2841.
(41) Zhao, J. Q.; Zhang, W.; Huq, A.; Misture, S. T.; Zhang, B. L.; Guo, S. M.; Wu, L. J.; Zhu, Y. M.; Chen, Z. H.; Amine, K.; Pan, F.; Bai, J. M.; Wang, F. *Adv. Energy Mater.* **2017**, *7*, 1601266.
(42) Song, B. H.; Li, W. D.; Yan, P. F.; Oh, S. M.; Wang, C. M.; Manthiram, A. *J. Power Sources* **2016**, *325*, 620.
(43) Larson, A. C.; Dreele, R. B. V. *General Structure Analysis System (GSAS), LAUR 86−748*; Los Alamos National Laboratory: Los Alamos, NM, 2000.
(44) Toby, B. H. *J. Appl. Crystallogr.* **2001**, *34*, 210.
(45) Qiu, X.; Thompson, J. W.; Billinge, S. J. L. *J. Appl. Crystallogr.* **2004**, *37*, 678.
(46) Billinge, S. J. L.; Levin, I. *Science* **2007**, *316*, 1699.
(47) Overy, A. R.; Cairns, A. B.; Cliffe, M. J.; Simonov, A.; Tucker, M. G.; Goodwin, A. L. *Nat. Commun.* **2016**, *7*, 10445.
(48) Proffen, T.; Billinge, S. J. L.; Egami, T.; Louca, D. *Z. Kristallogr. - Cryst. Mater.* **2003**, *218*, 132.
(49) Breger, J.; Dupre, N.; Chupas, P. J.; Lee, P. L.; Proffen, T.; Parise, J. B.; Grey, C. P. *J. Am. Chem. Soc.* **2005**, *127*, 7529.
(50) Lyu, Y. C.; Hu, E. Y.; Xiao, D. D.; Wang, Y.; Yu, X. Q.; Xu, G. L.; Ehrlich, S. N.; Amine, K.; Gu, L.; Yang, X. Q.; Li, H. *Chem. Mater.* **2017**, *29*, 9053.
(51) Ravel, B.; Newville, M. *J. Synchrotron Radiat.* **2005**, *12*, 537.
(52) Blochl, P. E. *Phys. Rev. B: Condens. Matter Mater. Phys.* **1994**, *50*, 17953.
(53) Kresse, G.; Joubert, D. *Phys. Rev. B: Condens. Matter Mater. Phys.* **1999**, *59*, 1758.
(54) Kresse, G.; Furthmuller, J. *Phys. Rev. B: Condens. Matter Mater. Phys.* **1996**, *54*, 11169.
(55) Kresse, G.; Furthmuller, J. *Comput. Mater. Sci.* **1996**, *6*, 15.
(56) Perdew, J. P.; Burke, K.; Ernzerhof, M. *Phys. Rev. Lett.* **1996**, *77*, 3865.
(57) Anisimov, V. I.; Zaanen, J.; Andersen, O. K. *Phys. Rev. B: Condens. Matter Mater. Phys.* **1991**, *44*, 943.
(58) Zhou, F.; Cococcioni, M.; Marianetti, C. A.; Morgan, D.; Ceder, G. *Phys. Rev. B: Condens. Matter Mater. Phys.* **2004**, *70*, 235121.
(59) Koyama, Y.; Arai, H.; Tanaka, I.; Uchimoto, Y.; Ogumi, Z. *Chem. Mater.* **2012**, *24*, 3886.
(60) Cao, T. T.; Shi, C. S.; Zhao, N. Q.; He, C. N.; Li, J. J.; Liu, E. Z. *J. Phys. Chem. C* **2015**, *119*, 28749.
(61) Nazri, G. A.; Pistoia, O. *Lithium Batteries: Science and Technology*; Kluwer Academic Publishers: Norwell, 2003.
(62) Li, X.; Ao, Z.; Liu, J.; Sun, H.; Rykov, A. I.; Wang, J. *ACS Nano* **2016**, *10*, 11532.
(63) Mairoser, T.; Mundy, J. A.; Melville, A.; Hodash, D.; Cueva, P.; Held, R.; Glavic, A.; Schubert, J.; Muller, D. A.; Schlom, D. G.; Schmehl, A. *Nat. Commun.* **2015**, *6*, 7716.
(64) Egami, T.; Billinge, S. J. L. *Underneath the Bragg Peaks: Structure Analysis of Complex Materials*; Oxford/Pergamon Press: New York, 2004.
(65) Platero-Prats, A. E.; Mavrandonakis, A.; Gallington, L. C.; Liu, Y. Y.; Hupp, J. T.; Farha, O. K.; Cramer, C. J.; Chapman, K. W. *J. Am. Chem. Soc.* **2016**, *138*, 4178.
(66) Hu, E.; Lyu, Y.; Xin, H. L.; Liu, J.; Han, L.; Bak, S. M.; Bai, J.; Yu, X.; Li, H.; Yang, X. Q. *Nano Lett.* **2016**, *16*, 5999.
(67) Kang, K.; Meng, Y. S.; Bréger, J.; Grey, C. P.; Ceder, G. *Science* **2006**, *311*, 977.

DOI: 10.1021/jacs.8b06150
J. Am. Chem. Soc. 2018, 140, 12484−12492